www.elsevier.com/locate/talanta

Novel Biomimetic Enzyme for Sensitive Detection of Superoxide Anions

Fang Peng, Tingting Xu, Fan Wu, Chunxue Ma, Yuhong Liu, Jianying Li, Bo Zhao, Chun Mao

PII: S0039-9140(17)30544-1
DOI: http://dx.doi.org/10.1016/j.talanta.2017.05.028
Reference: TAL17562

To appear in: *Talanta*

Received date: 21 January 2017
Revised date: 4 May 2017
Accepted date: 10 May 2017

Cite this article as: Fang Peng, Tingting Xu, Fan Wu, Chunxue Ma, Yuhong Liu, Jianying Li, Bo Zhao and Chun Mao, Novel Biomimetic Enzyme for Sensitiv Detection of Superoxide Anions, *Talanta* http://dx.doi.org/10.1016/j.talanta.2017.05.028

Novel Biomimetic Enzyme for Sensitive Detection of Superoxide Anions

Fang Peng[1,2], Tingting Xu[3], Fan Wu[1], Chunxue Ma[1], Yuhong Liu[1], Jianying Li[2]*, Bo Zhao[1], Chun Mao[1]*

[1]National and Local Joint Engineering Research Center of Biomedical Functional Materials, Jiangsu Key Laboratory of Biofunctional Materials, School of Chemistry and Materials Science, Nanjing Normal University, Nanjing, 210023, China

[2]Nephropathy Department, Qingdao Haici Medical Center, Qingdao, 266033, China

[3]State Key Laboratory of Materials-Oriented Chemical Engineering, College of Food Science and Light Industry, Nanjing Tech University, Nanjing, 211816, China.

*maochun@njnu.edu.cn (C. Mao),

shuxin600@163.com(J.Y. Li)

Abstract

Superoxide anion ($O_2^{\bullet-}$), one of the most active reactive oxygen species (ROS) in micro-environment of the human body, is involved in some diseases if there is excess $O_2^{\bullet-}$ associated with oxidative stress. Accurate detection of its concentration has important medical diagnostic significance. In this work, a new electrochemical sensor was designed and fabricated for sensitive detection based on Mn-superoxide dismutase (MnSOD) that decorated onto the surface of magnetic polymeric nanotubes by surface self-assembly processes. The composite nanotubes were characterized by transmission electron microscopy (TEM), fourier transform infrared spectroscopy (FTIR), Zeta potential analyzer, energy dispersive spectroscopy (EDS) and vibrating

sample magnetometer(VSM), and the biosensor exhibited excellent analytical performance, for example, the interference could be eliminated with high selectivity, the linear range from 0.15 to 3.0 μM with a detection limit of 0.0136 μM (S/N = 3), Cyclic voltammogram (CV) curves of the biosensor for 30 overlapping cycles showed the biosensor had a good cycle stability. Results indicated that the magnetic polymeric nanotubes that decorated by $Mn_3(PO_4)_2$ nanoparticles could effectively catalyze the dismutation of $O_2^{\bullet-}$ that attributed to its high surface areas and a large number of active sites of self-assembled $Mn_3(PO_4)_2$ nanoparticles. This method combining nanotechnology and self-assembly technique provided a new appropriate platform to design and fabricate electrochemical sensor with high performance.

Graphical abstract

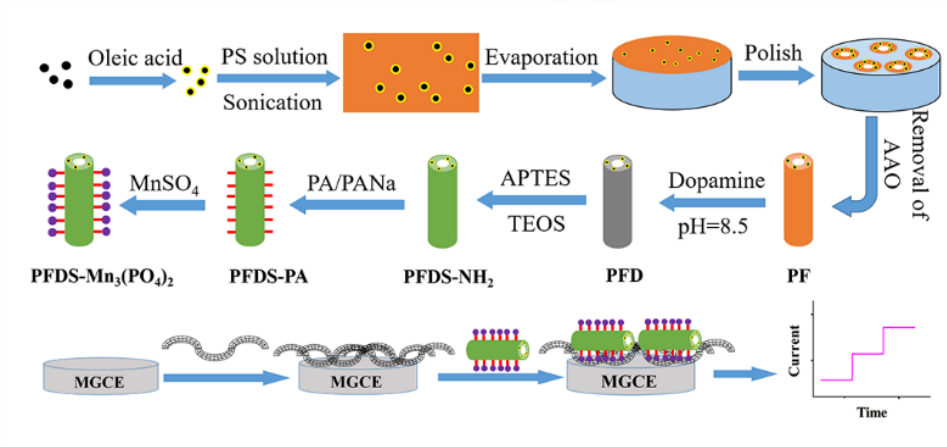

The schematic diagram was shown the formation of Fe_3O_4@PS/PDA/SiO_2-$Mn_3(PO_4)_2$ nanotubes and the stepwise construction process of modified magnetic glassy carbon electrode (MGCE) for detection of superoxide anions. The magnetic polymeric nanotubes that decorated by $Mn_3(PO_4)_2$ nanoparticles could effectively catalyze the dismutation of $O_2^{\bullet-}$ that attributed to its high surface areas and a large number of active sites of self-assembled $Mn_3(PO_4)_2$ nanoparticles.

This method combining nanotechnology and self-assembly technique provided a new appropriate platform to design and fabricate electrochemical sensor with high performance.

Keywords: Superoxide anion; Polystyrene nanotube; Manganous phosphate; Biomimetic enzyme; Electrochemical biosensor.

1. Introduction

At present, bioactive small molecules have attracted much attention due to their roles in biological processes, such as signaling molecules, biological tools, or therapeutic agents. The reactive oxygen species (ROS) are important cellular signaling species and inevitable products of the aerobic metabolism in cells, which could help to inhibit the propagation of bacterial and pathogenic fungi [1]. They are key intermediates in many toxicological mechanisms. Since superoxide anion ($O_2^{\bullet-}$) is the precursor of ROS, it is important to understand the relationship between $O_2^{\bullet-}$ fluxes and diseases [2-4]. Under normal metabolic conditions, $O_2^{\bullet-}$ is produced at a rate which should be matched by the capacity of tissue to catabolize them [5], however, excessive production of ROS would cause the oxidative stress and bring some diseases [1]. A great deal of evidence suggests that excessive production of ROS can be implicated in all kinds of diseases, including degenerative diseases and ischemia-reperfusion injury during surgery [2].

To date, all kinds of electrochemical enzyme sensors have been reported to detect $O_2^{\bullet-}$ through the use of specific enzyme catalysts such as cytochrome *c* and

superoxide dismutase (SOD) [5-9]. The direct electrochemistry of redox enzyme based on nanomaterials further improves the performance of superoxide anion radical sensors [10,11]. These enzyme-based biosensors, however, are limited from a very high cost and poor long-term stability as natural enzymes are prone to be denatured and lose their biological activity in adverse environment. Synthetic biomimetic enzyme is an alternative to detect superoxide anion by its catalytic dismutation of superoxide anion as a low cost synthetic enzyme while possession of wonderful stability [10,12,13]. McNaughton and Barnese were reported that manganese (Mn) compounds have proved to be reliable catalysts for $O_2^{\bullet-}$ [14,15]. Mn^{2+} was found to react fast with superoxide to produce the short-lived transient MnO_2^{+}. MnO_2^{+} was formed in the case of manganous phosphate and then was noticed to disproportionate fast by a second-order process to give manganous phosphate, hydrogen peroxide, and dioxygen [16]. Y. Luo et al. have reported a facile strategy for monitoring $O_2^{\bullet-}$ through direct electron transfer of manganese (II) phosphate ($Mn_3(PO_4)_2$) [17]. Li et al. have reported the above method requires potassium phosphate (K_3PO_4) in samples to provide phosphate ions for catalytic dismutation, thus greatly hindering its practical applications, especially for *in vivo* detection [10]. Zhou et al. have demonstrated a reliable and durable method for *in situ* real-time determination of $O_2^{\bullet-}$ based on direct electron transfer of $Mn_3(PO_4)_2$, which acted as a superoxide dismutase (SOD). Mn^{2+} was ion-exchanged into zeolite–ZSM-5 microstructures, and further coated with poly(diallyldimethylammonium chloride) (PDDA) [18]. Y. Luo et al. have developed a new electrochemical approach by immobilizing synthesized Mn-TPAA (TPAA,

tris[2-[N-(2-pyridylmethyl) amino] ethyl] amine) on TiO_2 nanoneedles surface for determination of $O_2^{\bullet-}$ [19]. Li has used DNA as a template to produce $Mn_3(PO_4)_2$ nanosheets and decorated this biomimetic enzyme onto the electrode surface for sensitive *in-situ* detection of $O_2^{\bullet-}$ [10]. However, the intrinsic drawbacks of DNA, including instability, and storage difficulty, may limit their widely applications of electrochemical sensors. A recent work reported a manganous phosphate ($Mn_3(PO_4)_2$) nanosheets-based biosensor developed to detect $O_2^{\bullet-}$ and researched the related catalytic mechanism [20]. However, it was reported that conventional synthesized MnSOD mimics with multilayer sheet structure **(**Figure S1) would bring resources waste and low catalytic efficiency [21]. Whether we were able to construct better forms of MnSOD mimics was the goal of this study.

In the past several years, the polymer nanotube, a new branch of nanotubes, has attracted quite a number of attention due to its prominent functions and special applications [22]. Until now, Nanotubes have been widely studied in many fields since they can be potentially used as drug carriers, chemical sensors, optoelectric nanodevices, and so on [23-25]. All sorts of polymer nanotubes have been prepared in many different ways. The template method, a simple and very effective method, is widely known [26]. Anodic aluminum oxide (AAO) template is often regarded as one of the most useful templates because it has homogeneous pores and can be removed conveniently [22]. Therefore, in this paper, the polystyrene nanotubes would be prepared by AAO template method as the carrier of $Mn_3(PO_4)_2$. Moreover, magnetic nanoparticles (MNPs) were embedded or encapsulated in the walls of the PS

nanotubes. Magnetic nanoparticles could be attracted by magnetic electrode with ease, which could reduce the loss of electrode surface modification material during the experiment and enhance the stability of the modified electrode [27].

The advances of nanoscience provide powerful tools to template or/and architect various materials for unique properties and superior nanostructures. Herein a novel electrochemical sensor was synthesized and further architected in nanoscales by $Mn_3(PO_4)_2$ self-assembly processes that occurred on the surface of magnetic polystyrene nanotubes for sensitive in situ detection of $O_2^{\bullet-}$, in which the magnetic polystyrene nanotubes with high specific surface areas and plenty of active sites of the self-assembled $Mn_3(PO_4)_2$ could effectively catalyze the dismutation of $O_2^{\bullet-}$. This approach might hold a great promise for widespread applications in drug discovery and clinic diagnostics.

2. Experiments

2.1. Materials

AAO template of 200 nm diameter pores was purchased from Whatman International Ltd. (U.K.). Polystyrene grains were purchased from Nanjing Yong Hong Chemical Co., Ltd. (Mw~231.9kg/mol, Mw/Mn=1.98). Multiwalled carbon nanotubes (MWCNTs) was obtained from Shenzhen Nanotech Port Co. Ltd. Toluene (AR), ammonium hydroxide solution ($NH_3 \cdot H_2O$) was obtained from Shanghai LingFeng Chemical Reagent Co. Ltd. Iron(II) chloride tetrahydrate ($FeCl_2 \cdot 4H_2O$) was obtained from Shanghai Richjoint Chemical Reagent Co., Ltd. Oleic acid (OA) was obtained from Aladdin. 18-crown-6, nafion (5 wt% solution in lower aliphatic

alcohol), phorbol 12-myristate 13-acetate (PMA), dopamine (DA), cysteine (Cys), ascorbic acid (AA) and uric acid (UA) were acquired from Aladdin Sigma-Aldrich Co. (USA). Iron (III) chloride hexahydrate ($FeCl_3 \cdot 6H_2O$), phytic acid solution (PA), ethyl silicate (TEOS), (3-aminopropyl) triethoxysilane, hexane, sodium hydroxide, dimethyl sulfoxide (DMSO) were purchased from Sinopharm Chemical Reagent Co., Ltd. Potassium hyperoxide (KO_2) was obtained from Alfa Aesar. Hydrogen peroxide (H_2O_2, 30%) was received from Beijing Chemical Works (China). Phosphate buffer solution (PBS) was obtained by dissolving 8.0 g NaCl, 0.2 g KCl, 0.24 g KH_2PO_4 and 1.44 g NaH_2PO_4 in 1000 mL double-distilled water. Sodium phytate was purchased from Shandong Xiya Chemical Industry Co., Ltd. Manganese sulfate monohydrate was purchased from Xilong Chemical Co., Ltd.

2.2. Preparation of oleic acid modified magnetic nanoparticles

The Fe_3O_4 nanoparticles were synthesized by precipitation of Fe (II) and Fe (III) in an alkaline solution. A total of 3 g of $FeCl_2 \cdot 4H_2O$ and 6.75 g of $FeCl_3 \cdot 6H_2O$ were dissolved in 75 mL of distilled water under nitrogen atmosphere at room temperature. Then 20 mL of ammonium hydroxide solution was added fast to the above solution under strong stirring to synthesize black precipitates. Three grams of oleic acid were added drop by drop at a certain rate to the solution that had been heated at 80°C for an hour. The mixture was cooled to room temperature after an hour of reaction, and the oleic acid modified magnetic fluid was collected magnetically and washed using hexane and ethanol repeatedly. Then the black slurry was further dispersed in hexane for storage [28,29].

2.3. Preparation of magnetic polystyrene nanotubes

The polystyrene/toluene solution was prepared by dissolving 1 g polystyrene grains in 20 ml toluene, and mixed with the oleic acid modified magnetic nanoparticles (0.45 g) by sonication for an hour. A drop of the polystyrene/toluene solution was placed on a microscope slide, on which a commercial AAO template was fast placed. The polystyrene/toluene solution entered the AAO template pores completely along their inner wall merely in several seconds. Twelve hours later the solvent was almost completely evaporated at room temperature. The AAO/magnetic polystyrene composite membrane was removed from the microscope slide, and then the composite membrane was polished by 1000 mesh sandpaper. Afterwards the composite membrane was submerged in the 3 M sodium hydroxide solution to dissolve the AAO template and the Fe_3O_4@PS nanotubes were obtained [22,29-31].

2.4. Preparation of Fe_3O_4@PS/PDA/SiO_2-$Mn_3(PO_4)_2$ nanotubes

In order to coat magnetic polystyrene nanotubes with the PDA layer, 4 mg of magnetic polystyrene nanotubes and 16 mg of dopamine hydrochloride were dissolved in 8 mL buffer solution of Tris (10 mM, pH = 8.5). After 24 hours of oscillation at room temperature, the synthetic products were separated by an external magnet and washed several times with ethanol and ultrapure water. Finally, they were dried at room temperature for 24 hours in a vacuum oven [29,32,33]. 4 mg of Fe_3O_4@PS/PDA nanotubes were dissolved in 20 mL deionized water, and then added with 40 μL of TEOS for postcoating and surface modification. At room temperature, the above solution was then subjected to mechanical stirring for 30 minutes. The

active functional groups grafted onto the surface of the Fe_3O_4@PS/PDA/SiO_2 nanotubes were synthesized by condensation of TEOS and 40 μL of APTES. Then 50 μL buffer solution of PA/PA sodium salt hydrate (pH = 7) was added into the above solution and continued stirring for 24 hours. The obtained product was washed with alcohol and deionized water several times and finally dried overnight at 60 °C under vacuum. Finally, the Fe_3O_4@PS/PDA/SiO_2-PA nanotubes were redispersed in 10 mL of deionized water. Subsequently, $MnSO_4$ aqueous solution (10 mL, 12 mM) was added to the three-necked flask containing the Fe_3O_4@PS/PDA/SiO_2-PA nanotubes under continuous stirring for 2 hours at a temperature of 60 °C. After the reaction, the product was collected through centrifugation, washed with deionized water several times, and dried for 24 hours in a vacuum oven at a temperature of 60°C [10,21,34,35].

2.5. Fabrication of Fe_3O_4@PS/PDA/SiO_2-$Mn_3(PO_4)_2$/MWCNTs/MGCE

Magnetic glass carbon electrode (MGCE d = 3 mm) was carefully polished with 0.3 μm and 0.05 μm of alumina aqueous slurry to a mirror-like surface. Then it was washed ultrasonically in ultrapure water and ethanol severally and dried under purged nitrogen at room temperature [27].

0.5 g of MWCNT and concentrated sulfuric acid (40 mL) and concentrated nitric acid (40 mL) (the volume ratio was 1:1) were placed in a 250 mL three-necked round-bottom flask followed by constantly stirring at a temperature of 120 °C in an oil bath for 6 hours under reflux of water. Then the above acid solution was centrifuged at 10000 r/min and washed with deionized water until the solution

reached neutral. Then the product was dried in an oven at a temperature of 100°C for 24 hours [10].

Subsequently, MWCNTs (8.0 μL, 0.5 $mg \cdot mL^{-1}$) were dropped onto the magnetic electrode surface and dried under purged nitrogen at room temperature. After that, Fe_3O_4@PS/PDA/SiO_2-$Mn_3(PO_4)_2$ nanotubes (8.0 μL，2.0 $mg \cdot mL^{-1}$) and 2.5% Nafion were mixed with the volumetric ratio of 1:1, and 8.0 μL of above mixture was dropped onto the surface of MWCNTs/MGCE. The Fe_3O_4@PS/PDA/SiO_2-$Mn_3(PO_4)_2$/MWCNTs/MGCE was obtained after drying for several hours in air. The modified magnetic electrodes were stored at 4°C until use during the experiment [21].

2.6. Culture of Cells

The HeLa cells grown in Dulbecco's Modified Eagle's medium (DMEM) supplemented with 10% fetal bovine serum (FBS), 100 $\mu g \cdot mL^{-1}$ streptomycin, and 100 $units \cdot mL^{-1}$ penicillin at a temperature of 37°C in a humidified incubator (95% air with 5% CO_2). The HeLa cells were centrifuged for the subsequent electrochemical experiments. Real sample were measured by adding 100 $\mu g \cdot mL^{-1}$ PMA in PBS containing 50 mM glucose [21,36].

2.7. In situ Detection of Extracellular $O_2^{\bullet -}$

For the detection of $O_2^{\bullet -}$ released from living HeLa cells, 2 mL 0.1 M PBS (pH = 7.4) solution (with or without 0.5×10^5 $cells \cdot mL^{-1}$) was used for real sample measurements and was gently stirred for $O_2^{\bullet -}$ uniformly distributed for accurate measurements [10].

2.8. Instrumentation

Transmission electron microscopy (TEM) (HITACHI H-7650, Japan) was designed to observe their morphology. EDS measurements were performed on the scanning electron microscopy (SEM, LEO1530VP, Germany) was equipped with an energy dispersive X-ray analysis. The Fe_3O_4@PS/PDA/SiO_2 nanotubes were also measured using Transform Infrared Spectroscopy (FT-IR, Tensor 27, Bruker, Germany). Magnetic analysis of Fe_3O_4@PS/PDA/SiO_2-$Mn_3(PO_4)_2$ nanotubes was performed using the vibrating sample magnetometer (LakeShore VSM 7404, USA). All the electrochemical data were analyzed by CHI 760D electrochemical workstation (Shanghai Chenhua, China). Surface potential of the samples was analyzed by Zeta potential analyzer (Malvern Instruments ZS90). All electrochemical experiments were performed using a three-electrode cell equipped, which included saturated calomel electrode (SCE), magnetic glass carbon electrode (MGCE) and a platinum electrode.

3. Results and Discussion

3.1 Mechanism of the Fe_3O_4@PS/PDA/SiO_2-$Mn_3(PO_4)_2$ nanotubes sensor

Figure 1. Schematic illustration of (A) the formation of Fe_3O_4@PS/PDA/SiO_2-$Mn_3(PO_4)_2$ nanotubes (PF: Fe_3O_4@PS nanotube; PFD: Fe_3O_4@PS/PDA nanotube; PFDS-NH_2: Fe_3O_4@PS/PDA/SiO_2-NH_2 nanotube; PFDS-PA: Fe_3O_4@PS/PDA/SiO_2-PA nanotube; PFDS-$Mn_3(PO_4)_2$: Fe_3O_4@PS/PDA/SiO_2-$Mn_3(PO_4)_2$ nanotube), (B) Preparation procedures of Fe_3O_4@PS/PDA/SiO_2-$Mn_3(PO_4)_2$ nanotubes sensor for detection of superoxide

anions.

Figure 1A illustrated the procedure of preparing Fe_3O_4@PS/PDA/SiO_2-$Mn_3(PO_4)_2$ nanotubes consisted of two steps. The first step was to synthesize Fe_3O_4@PS/PDA nanotubes of a wonderful physical and mechanical property with polystyrene/toluene solution containing good dispersion of oleic acid modified magnetic particles in a AAO template (200 nm pores) through a simple physical method. In order to improve the magnetic nanoparticles better dispersion in the polystyrene/toluene solution, Fe_3O_4 nanoparticles modified with oleic acid were introduced. Due to the hydrophobic properties, the magnetic nanoparticles could be dispersed well in the polystyrene/toluene solution [28]. The oleic acid modified Fe_3O_4 nanoparticles with hydrophobic property were completely dispersed in the polystyrene/toluene solution during the experiments. Consequently, after the solvent had evaporated, the Fe_3O_4 nanoparticles were embedded or encapsulated in the polystyrene nanotubes. Lee et al. recently reported a new method to construct multifunctional polymer coatings by simple dip-coating of objects in an aqueous solution of dopamine [32]. In general, in the presence of oxygen and under weak alkaline aqueous conditions at room temperature, dopamine can self-polymerize to get polydopamine (PDA), which spontaneously deposits a thin adherent coating onto all sorts of material surfaces, having similar functions to the adhesive foot proteins secreted by mussels [37]. More importantly, the PDA layer could be used as a multifunctional platform for secondary reactions [38]. Secondary reactions could be used to generate various ad-layers, including metal films through electroless metallization, self-assembled monolayers by

deposition of long-chain molecular building blocks, and bioactive and bioinert surfaces through grafting of macromolecules [32]. Dopamine coating and surface modification was a kind of versatile green chemistry method because of simple ingredients, mild reaction conditions, inexpensiveness, and PDA could adsorb various substances effectively through covalent or non-covalent force [27,39]. And then, by simple dip-coating of objects in an alkaline aqueous solution of dopamine, Fe_3O_4@PS/PDA nanotubes were easy to obtain [32]. The second step was to use the easy and feasible method to prepare silica-coated Fe_3O_4@PS/PDA nanotubes by the sol-gel chemistry [34,40]. Phytic acid (PA) was a well-known naturally occurring acid and biocompatible, nontoxic, and "green" to the environment. Phytic acid had six acid groups attached symmetrically to a cyclohexanehexol ring in structure and phytic acid was usually negatively charged [41,42]. After dropping into phytic acid / phytic acid sodium salt hydrate buffer solution (pH = 7), PO_4^{3-} ions were coupled with Fe_3O_4@PS/PDA/SiO_2-NH_2 nanotube by electrostatic interaction to form Fe_3O_4@PS/PDA/SiO_2-PA nanotube. Due to its unique structure and property, phytic acid had a strong tendency to interact or couple with positively charged metal ions [41]. $Mn_3(PO_4)_2$ molecular was self-assembly on the outer surface of Fe_3O_4@PS/PDA/SiO_2-PA nanotubes when the PO_4^{3-} ions were consumed [21]. A schematic illustration of the stepwise construction process of modified magnetic glassy carbon electrode (MGCE) was shown in Figure 1B. After introducing MWCNTs, the highly conductive MWCNTs could considerably improve electron transfer between the electrode and the biomimetic enzyme, enabled quantitative

detection of $O_2^{\bullet-}$ released from cancer cells with excellent selectivity, high sensitivity, and fast response and thus rendered a helpful tool to explore the crucial role of $O_2^{\bullet-}$ in all kinds of pathological and physiological processes.

3.2. Characterization of nanotubes

3.2.1. Morphological characterization of various PS nanotubes

Figure 2. Transmission electron microscopy (TEM) images of PS nanotube (A), Fe_3O_4 nanoparticles (B), Fe_3O_4@PS nanotube (C), Fe_3O_4@PS/PDA nanotube (D), Fe_3O_4@PS/PDA/SiO_2-NH_2 nanotubes (E and F), Fe_3O_4@PS/PDA/SiO_2-PA nanotube (G)，Fe_3O_4@PS/PDA/SiO_2-$Mn_3(PO_4)_2$ nanotube (H).

Figure 2A showed TEM image of polystyrene nanotube prepared by wetting AAO template. We could notice that the nanotube with an average diameter of 200 nm was synthesized by 5 wt% polystyrene/toluene solution, and the wall thickness of the polystyrene nanotube was about 50 nm. The oleic acid modified magnetic nanoparticles were about 5 nm in size as revealed by TEM. (Figure 2B). In contrast, the Fe_3O_4@PS nanotube had an apparent hollow structure with a diameter of about 200 nm (Figure 2C). As presented in Figure 2D, Fe_3O_4@PS nanotube was wrapped by a certain polymer shell, which had lighter color than that of the sidewall of Fe_3O_4@PS nanotube. Dopamine was expected to be self-polymerized on the surface of the polystyrene nanotubes when mixed with the polystyrene nanotubes overnight at a pH of 8.5 [43]. Previously magnetically separated nanotube was coated with PDA, which appeared to be a little thicker. As shown in Figure 2E and Figure 2F, we could

observe that the silica shells of the Fe_3O_4@PS/PDA/SiO_2-NH_2 nanotubes surface were so clear, and Fe_3O_4@PS/PDA/SiO_2-NH_2 nanotube became thicker. After surface self-assembly of phytic acid and free divalent manganese ions sequentially, the two sizes of Fe_3O_4@PS/PDA/SiO_2-PA nanotube and Fe_3O_4@PS/PDA/SiO_2-$Mn_3(PO_4)_2$ nanotube showed a slight increase (Figure 2G, 2H), respectively.

3.2.2. Zeta potential and FTIR spectra analysis

Figure 3. (A) The Zeta potential analysis of (a) Fe_3O_4@PS/PDA nanotubes, (b) Fe_3O_4@PS/PDA/SiO_2-NH_2 nanotubes, (c) Fe_3O_4@PS/PDA/SiO_2-PA nanotubes, and (d) Fe_3O_4@PS/PDA/SiO_2-$Mn_3(PO_4)_2$ nanotubes. (B) FTIR spectra of (a) PS nanotubes (b) Fe_3O_4@PS/PDA nanotubes, (c) Fe_3O_4@PS/PDA/SiO_2-NH_2 nanotubes, and (d) Fe_3O_4@PS/PDA/SiO_2-PA nanotubes.

The zeta potential of different nanotubes as shown in Figure 3A, the Zeta potential of Fe_3O_4@PS/PDA nanotubes surface (column a) was - 16.58 ± 0.83 mV, which was due to the protonation/deprotonation of the phenolic and amino groups of PDA [44]. When modified with APTES, the Zeta potential of Fe_3O_4@PS/PDA/SiO_2-NH_2 nanotubes increased to + 24.42 ± 1.30 mV that due to the amine groups on the surface of the nanotubes (column b). However, the Zeta potential measurements for Fe_3O_4@PS/PDA/SiO_2-PA nanotubes (column c) was - 27.25 ± 1.73 mV, which due to the six phosphate groups of phytic acid. The zeta potential increased to - 7.63 ± 0.46 mV when a large amount of Mn^{2+} ions in solution were self-assembled onto the surface of Fe_3O_4@PS/PDA/SiO_2-PA nanotubes (column d). The change of Zeta

potential demonstrated that Fe_3O_4@PS/PDA/SiO_2-$Mn_3(PO_4)_2$ nanotubes were successfully synthesized through self-assembly technology based on the electrostatic interaction that between the phosphate groups and Mn^{2+} ions.

As shown in Figure 3B, typical polystyrene absorption bands at around 698, 757, 1029, 1450, 1494, 1601, 2922 and 3026 cm^{-1} could be observed clearly in the FTIR spectrum of the polystyrene nanotubes before the surface modification with polydopamine (curve a). After the surface had been coated with polydopamine, several new absorbance bands appear, as shown in curve b. The broad band absorbance between 3600 and 3100 cm^{-1} was attributed to N−H/O−H stretching vibrations from polydopamine, at the wavenumber of 1496 cm^{-1}, the peak intensity in Fe_3O_4@PS/PDA nanotubes was obviously higher than that in the PS nanotubes, and the bands at 1496 cm^{-1} and 1296 cm^{-1} were attributed to the shearing vibration of amide N−H and stretching vibration of the phenolic C−OH of the polydopamine, respectively [33,37]. Polydopamine gave bands at the wavenumber of 1336 cm^{-1} and 815 cm^{-1}, resulting from stretching and deformation of aromatic rings [43]. These FTIR results demonstrated the successful synthesis of the surface-adherent polydopamine coatings onto the surfaces of PS nanotubes through dopamine self-polymerization. For curve c, two bands appeared around at the wavenumber of 1159 cm^{-1} and 973 cm^{-1} were due to the O−Si−O bonds stretching vibration, which indicated that silica layer were successfully synthesized. Compared with Fe_3O_4@PS/PDA nanotubes (curve b), Fe_3O_4@PS/PDA/SiO_2-NH_2 nanotubes (curve c) showed a new absorption at the wavenumber of 2958 cm^{-1} most probably coming

from stretching vibration of −C−NH_2, which indicated that the successful functionalization of APTES on the surface of Fe_3O_4@PS/PDA/SiO_2 nanotubes [21,35,45]. Moreover, the intensity of the peak (curve d) at the wavenumber of 1159 cm^{-1} increased due to the phosphate bands of phytic acid and the overlap of these phosphate bands with the O−Si−O bands [35,46]. This demonstrated that phytic acid successfully modified onto the surface of Fe_3O_4@PS/PDA/SiO_2−NH_2 nanotubes through electrostatic interaction.

3.2.3. Magnetic analysis and the energy dispersive spectroscopy (EDS) measurements

Figure 4. Magnetic hysteresis loops of (a) oleic acid modified Fe_3O_4 nanoparticles and (b) Fe_3O_4@PS/PDA/SiO_2-$Mn_3(PO_4)_2$ nanotubes.

As shown in Figure S2, after the MWCNTs modified magnetic electrode was inserted into the solution, a lot of Fe_3O_4@PS/PDA/SiO_2-$Mn_3(PO_4)_2$ nanotubes could be attracted on the surface of the MWCNTs modified magnetic electrode. The magnetic hysteresis loops obtained from the oleic acid modified Fe_3O_4 nanoparticles and Fe_3O_4@PS/PDA/SiO_2-$Mn_3(PO_4)_2$ nanotubes were shown in Figure 4. The saturation magnetization values of the oleic acid modified Fe_3O_4 nanoparticles and Fe_3O_4@PS/PDA/SiO_2-$Mn_3(PO_4)_2$ nanotubes were 65.51 emu/g and 24.70 emu/g, respectively.

In addition, SEM images and energy dispersive spectroscopy (EDS) measurements were performed to obtain the characterizations of Fe_3O_4@PS nanotubes and

Fe_3O_4@PS/PDA/SiO_2-$Mn_3(PO_4)_2$ nanotubes. Figure S3 showed SEM image and EDS measurements of Fe_3O_4@PS nanotubes. As shown in Figure S4, it can be observed that magnetic nanoparticles were densely embedded or encapsulated in the walls of the PS nanotubes. Figure S5A showed SEM image of Fe_3O_4@PS/PDA/SiO_2-$Mn_3(PO_4)_2$ nanotubes. Figure S5B showed that the different atomic percentages were 60.39% (C), 8.60% (N), 24.52% (O), 2.27% (Si), 1.96% (P), 2.15% (Mn), and 0.01% (Fe), respectively. It could be proved that $Mn_3(PO_4)_2$ was firmly coated onto the outer surface of the Fe_3O_4@PS/PDA/SiO_2-PA nanotubes (see Supporting Information for details).

3.3. Electrochemical characterization

Figure 5. Cyclic voltammograms (CVs) of various electrodes in the absence (A) and presence (B) of 1.0 μmol L^{-1} $O_2^{\bullet-}$ in PBS (pH = 7.4), scan rate: 100 $mV{\cdot}s^{-1}$((a) bare MGCE, (b) Fe_3O_4@PS/PDA/SiO_2-NH_2/MGCE, (c) Fe_3O_4@PS/PDA/SiO_2-$Mn_3(PO_4)_2$/MGCE, (d) MWCNTs/MGCE, and (e) Fe_3O_4@PS/PDA/SiO_2-$Mn_3(PO_4)_2$/MWCNTs/MGCE), (C) The Nyquist plots of (a) bare MGCE, (b) MWCNTs/MGCE, (c) Fe_3O_4@PS/PDA/SiO_2-$Mn_3(PO_4)_2$/MWCNTs/MGCE, and (d) Fe_3O_4@PS/PDA/SiO_2-$Mn_3(PO_4)_2$/MGCE in the presence of 10 mM of $[Fe(CN)_6]^{3-/4-}$ and 0.1 M KCl, (D) Schematic illustration of $O_2^{\bullet-}$ dismutation catalyzed by Mn^{2+}/MnO_2^{+} confined into the magnetic electrode surface.

Cyclic voltammetry was applied to research the electrocatalytic property of the

Fe_3O_4@PS/PDA/SiO_2-$Mn_3(PO_4)_2$ nanotubes sensing platform. Figure 5A showed that all synthesis process of Fe_3O_4@PS/PDA/SiO_2-$Mn_3(PO_4)_2$/MWCNTs/MGCE were tested by CV in nitrogen saturated phosphate buffered solution at a scanning rate of 100 $mV \cdot s^{-1}$. In the working potential range of 0 ~ 0.9 V, there were no obvious electrochemical responses can be obtained at the bare MGCE (curve a), Fe_3O_4@PS/PDA/SiO_2-NH_2/MGCE (curve b), and MWCNTs/MGCE (curve d). Conversely, the Fe_3O_4@PS/PDA/SiO_2-$Mn_3(PO_4)_2$/MGCE showed a pair of weakly redox peaks (curve c). When the MWCNTs/MGCE was modified with Fe_3O_4@PS/PDA/SiO_2-$Mn_3(PO_4)_2$ nanotubes, the response was much stronger than that of Fe_3O_4@PS/PDA/SiO_2-$Mn_3(PO_4)_2$ nanotubes modified MGCE (curve e). This might be due to wonderful electronic conductivity of MWCNTs, which would greatly improve the sensitivity of analysis [47]. As shown in Figure 5B, in the presence of 1.0 μmol L^{-1} $O_2^{\bullet-}$ in the PBS, both cathodic and anodic peak currents that corresponding to the redox reaction of in PBS obviously enhanced that could be due to the oxidation and reduction of $O_2^{\bullet-}$, respectively. The comparison of the two conditions was shown in Figure S6. The CV results clearly demonstrated that the catalytic activity of the biomimetic enzyme $Mn_3(PO_4)_2$ towards the dismutation of $O_2^{\bullet-}$ was retained in the nanotubes, and the electron transfer between the underlying electrode and $Mn_3(PO_4)_2$ was efficiently mediated through the conductive MWCNTs, which was indicated that the Fe_3O_4@PS/PDA/SiO_2-$Mn_3(PO_4)_2$/MWCNTs/MGCE was an efficient biosensor for $O_2^{\bullet-}$ detection. Figure 5C showed the Nyquist diagrams of the bare MGCE, MWCNTs/MGCE, Fe_3O_4@PS/PDA/SiO_2-$Mn_3(PO_4)_2$/MWCNTs/MGCE and

Fe_3O_4@PS/PDA/SiO_2-$Mn_3(PO_4)_2$/MGCE. The impedance spectrum of the bare MGCE was demonstrated in (curve a). When MWCNTs was modified on the MGCE (curve b), there was almost a small semicircle domain in the Nyquist diagrams, indicating that MWCNTs showed excellent conductivity. After the Fe_3O_4@PS/PDA/SiO_2-$Mn_3(PO_4)_2$ was coated on the MWCNTs/MGCE, the semicircle domain expanded (curve c) because of the weak electrical conductivity of Fe_3O_4@PS/PDA/SiO_2-$Mn_3(PO_4)_2$ nanotubes. The resistance of the composite greatly increased (curve d) when only Fe_3O_4@PS/PDA/SiO_2-$Mn_3(PO_4)_2$ nanotubes were coated on the MGCE. The inset of Figure 5C displayed the equivalent circuit of the electrochemical system which involved charge-transfer resistance (R_{ct}), Warburg impedance (Z_w), solution resistance (R_s) and double layer capacitance (C_d). The Nyquist diagrams (Figure 5C) fitted well to an equivalent circuit presented in the inset. The values of the item of the equivalent circuit were summarized in Table S1. From Table S1, the charge-transfer resistances (Rct) of (a) bare MGCE, (b) MWCNTs/MGCE, (c) Fe_3O_4@PS/PDA/SiO_2-$Mn_3(PO_4)_2$/MWCNTs/MGCE, and (d) Fe_3O_4@PS/PDA/SiO_2-$Mn_3(PO_4)_2$/MGCE were calculated to be 87.48 Ω, 114.3 Ω, 246.7 Ω and 642 Ω, respectively, which was consistent with the result of the Nyquist diagrams.

In order to research the catalysis effect of the Fe_3O_4@PS/PDA/SiO_2-$Mn_3(PO_4)_2$ nanotubes, the biosensor in PBS and PBS of containing 1.0 μmol L^{-1} of $O_2^{\bullet-}$ were tested through CVs, respectively. As shown in Figure S6, in the presence of 1.0 μmol L^{-1} $O_2^{\bullet-}$ in the PBS, both cathodic and anodic peak currents that corresponding to the

redox reaction of in PBS obviously enhanced that could be due to the oxidation and reduction of $O_2^{\bullet-}$, respectively. According to the previous reports [18,48], in PBS, $O_2^{\bullet-}$ was converted into H_2O_2 and O_2 during the period of disproportionation reaction that $O_2^{\bullet-}$ was catalyzed by Mn^{2+} ions. $O_2^{\bullet-}$ was oxidized to O_2 through the oxidation of MnO_2^+, while MnO_2^+ was reduced back to Mn^{2+} in the anodic process. On the contrary, Mn^{2+} was considered to be oxidized to MnO_2^+ in the cathodic process. The proposed electrode reaction mechanisms for the anodic and cathodic process were shown in Figure 5D. We considered these two redox processes separately by fabricating two electrodes on which each reaction occurred separately.

The anodic process:

$$Mn^{2+} - e \rightarrow MnO_2^+$$

$$MnO_2^+ + O_2^{\bullet-} \rightarrow Mn^{2+} + O_2$$

The cathodic process:

$$MnO_2^+ + e \rightarrow Mn^{2+}$$

$$Mn^{2+} + O_2^{\bullet-} + 2H^+ \rightarrow MnO_2^+ + H_2O_2$$

Furthermore, by comparing Figure 5A (curve c, e) with Figure 5B (curve c, e), both the cathodic and anodic peak currents that corresponding to the redox reaction of in PBS obviously enhanced that could be due to the oxidation and reduction of $O_2^{\bullet-}$, respectively. These results indicated that the obvious increases in the anodic and cathodic peak currents could be ascribed to the mediation of Fe_3O_4@PS/PDA/SiO_2-$Mn_3(PO_4)_2$ for the dismutation of $O_2^{\bullet-}$. As discussed above, the Fe_3O_4@PS/PDA/SiO_2-$Mn_3(PO_4)_2$/MWCNTs/MGCE could be used to detect $O_2^{\bullet-}$

through measuring the oxidation or reduction currents due to the high efficient catalysis of Fe_3O_4@PS/PDA/SiO_2-$Mn_3(PO_4)_2$ nanotubes.

3.4. Current-time curve and linear calibration plot

Figure 6. (A) Continuous amperometric responses of Fe_3O_4@PS/PDA/SiO_2-$Mn_3(PO_4)_2$/MWCNTs/MGCE obtained at 0.580 V in PBS (pH = 7.4), from 0.15 to 3.0 μM, the $O_2^{\bullet-}$ concentration of each adding step was 0.15 μM. (B) Linear calibration plot of the response current versus the $O_2^{\bullet-}$ concentration.

The typical current-time curve of Fe_3O_4@PS/PDA/SiO_2-$Mn_3(PO_4)_2$/MWCNTs/M-GCE at the applied potential of 0.580 V upon continuous additions of $O_2^{\bullet-}$ was showed in Figure 6A. While being mildly stirred, $O_2^{\bullet-}$ solution was added once per 50 seconds in this experiment. The response displayed a linearly increase process with an increase in $O_2^{\bullet-}$ concentration from 0.15 and 3.0 μmol L^{-1} with the linear correlation coefficient of 0.99762. The relationship between the oxidation peak current and the concentration of $O_2^{\bullet-}$ was linear with a detection limit of 0.0135 μM (S/N = 3). The corresponding calibration plot for $O_2^{\bullet-}$ were recorded in Figure 6B. The corresponding linear equations was I (μA) = 0.03109 + 0.10245c (μM). The biosensor was used to the detection of $O_2^{\bullet-}$ and showed wonderful electrochemical performance.

3.5. Anti-interference performance

Figure 7. Current responses (A) and histogram profile (B) of

Fe_3O_4@PS/PDA/SiO_2-$Mn_3(PO_4)_2$/MWCNTs/MGCE for the assaying of $O_2^{\bullet-}$ against the diverse interferes.

The biosensor could be applied to evaluate the anti-interference performance of detecting $O_2^{\bullet-}$, and it was measured by continuous additions of $O_2^{\bullet-}$ and interfering substances into a 0.1 M PBS at 0.580 V (Figure S7). Figure 7A indicated that there were significant current responses of the biosensor during the addition of 1.0 μM $O_2^{\bullet-}$, while no significant current response could be changed with the additional interferences. With the sequential addition of 10 μM UA, 5.0 μM DA, 5.0 μM Cys, 10 μM AA and 10 μM H_2O_2, the detection current revealed changes of 6.3%, 11.7%, 12.5%, 9.4% and 3.1% with comparison of 1.0 μM $O_2^{\bullet-}$, respectively (Figure 7B).

Figure S8 showed the amperometric response of the Fe_3O_4@PS/PDA/SiO_2-$Mn_3(PO_4)_2$/MWCNTs/MGCE by continuous additions of 2.0 μM 18-crown-6 once per 50 seconds. Results indicated that this biosensor could restrain many kinds of interference and demonstrate an excellent activity and selectivity for detection of $O_2^{\bullet-}$.

3.6. Application in real samples

Figure 8. Amperometric response of the Fe_3O_4@PS/PDA/SiO_2-$Mn_3(PO_4)_2$/MWCNTs/MGCE in the (A) absence, and (B) presence of HeLa cells upon continuous additions of PMA to 0.1 M PBS at 0.580V.

The biomimetic enzyme sensor was further applied to test $O_2^{\bullet-}$ released from the HeLa cells. The amperometric responses of the biosensor were recorded in 2 mL 0.1

M PBS (pH = 7.4) containing 0.5×10^5 cells·mL^{-1}. As shown in Figure 8, the sensor in the HeLa cell suspension displayed a significant enhancement of the current response at 0.580V (versus Hg/Hg_2Cl_2) with the addition of 4 μL 100 μg mL^{-1} phorbol 12-myristate 13-acetate (PMA), which was reported to active NADPH oxidase (endogenous) and induce $O_2^{\bullet-}$ generation from cells [49,50]. Thus, the enhanced response was attributed to the biomimetic catalytic reduction of superoxide anion released from living cells. Figure 8 showed that the varying current signal (0.023 μA, curve B) was caused by $O_2^{\bullet-}$ released from the HeLa cells, considering that Fe_3O_4@PS/PDA/SiO_2-$Mn_3(PO_4)_2$ nanotubes could selectively decompose $O_2^{\bullet-}$. The $O_2^{\bullet-}$ concentration of 0.079 μM was calculated on the basis of the above linear relationship. Therefore, the total amount of $O_2^{\bullet-}$ releasing from per 10^5 cells could be calculated to be 0.158 nmol. However, there was not affected by treatment with PMA in the absence of the HeLa cells，no obvious current response could be observed on the graph (curve A).

3.7. Cycle stability and optimization condition

As shown in Figure S9, the CV curves of the biosensor for 30 cycles, which showed nearly overlap curves, indicating that the biosensor we fabricated had good cycle stability that could be due to the good binding state of the Fe_3O_4@PS/PDA/SiO_2-$Mn_3(PO_4)_2$/MWCNTs/MGCE electrode. When the electrode was not in use, it was stored in refrigerator at 4℃. The electrode was measured after preparation and four weeks later. The results were shown in Figure S10, which indicated that the current response was no apparent decrease. After four weeks, the

obtained current response remained 95.8% of its initial current response, suggesting the stability of the electrode was also good.

The optimization results obtained with adjustment of the ratio of Fe_3O_4@PS/PDA/SiO_2-$Mn_3(PO_4)_2$ nanotubes to MWCNTs further demonstrated the important role of Fe_3O_4@PS/PDA/SiO_2-$Mn_3(PO_4)_2$ solution concentration for the performance of Fe_3O_4@PS/PDA/SiO_2-$Mn_3(PO_4)_2$/MWCNTs/MGCE. MWCNTs suspension (5 μL, 0.5mg/mL) was slowly dropped onto the pretreated MGCE and the electrode was dried under purged nitrogen at room temperature to obtain MWCNTs modified electrode [36]. The solution concentration effect on the electrochemical performance of the Fe_3O_4@PS/PDA/SiO_2-$Mn_3(PO_4)_2$/MWCNTs/MGCE was measured. The CVs of the magnetic electrode in solutions with different Fe_3O_4@PS/PDA/SiO_2-$Mn_3(PO_4)_2$ solution concentration were shown in Figure S11. The optimum concentration of Fe_3O_4@PS/PDA/SiO_2-$Mn_3(PO_4)_2$ nanotubes solution was found to be 2 mg/mL. However, the excess Fe_3O_4@PS/PDA/SiO_2-$Mn_3(PO_4)_2$ nanotubes could disturb the electron transfer between Fe_3O_4@PS/PDA/SiO_2-$Mn_3(PO_4)_2$ nanotubes and electrode.

Figure S12 showed that the peak currents of Fe_3O_4@PS/PDA/SiO_2-$Mn_3(PO_4)_2$/MWCNTs/MGCE (curve A) were a little larger than that of $Mn_3(PO_4)_2$/MWCNTs/MGCE (curve B). Results displayed that the electrocatalytic effect of Fe_3O_4@PS/PDA/SiO_2-$Mn_3(PO_4)_2$ nanotubes was a little higher than that of $Mn_3(PO_4)_2$ aggregated particles. This might primarily be attributed to that the nano-scale formulation of Fe_3O_4@PS/PDA/SiO_2-$Mn_3(PO_4)_2$ nanotubes

possessed high specific surface area. Therefore, it would help to improve the catalytic efficiency of $O_2^{\bullet-}$ in the electrolyte.

The biosensor displayed more excellent analytical performance than some $O_2^{\bullet-}$ biosensors that reported by the previous papers. Table 1 displayed the comparison of the analytical performance of various electrodes for $O_2^{\bullet-}$ detection.

Table 1. Comparison of the analytical performance of various electrodes for $O_2^{\bullet-}$ detection.

Electrode	Linear range (μM)	Detection Limit (μM)	Correlation coefficient	Ref.
Fe_3O_4@PS/PDA/SiO_2-$Mn_3(PO_4)_2$ /MWCNTs/MGCE	0.15 - 3.0	0.0136	0.9976	This work
Mn^{2+}-ZSM/PDDA/GCE	0.5 - 1200	0.37	-	[18]
MWCNTs/$Mn_2P_2O_7$-formylstyrylpyridine/GCE	0.08 - 3.19	0.029	0.9915	[36]
SOD/Pt-Pd/MWCNTs/SPGE	40 - 1550	0.71	0.9941	[51]
PMMA/PANI-Au_{nano}/SOD-ESCFM	0.5 - 2.4	0.3	0.9944	[52]
((SOD/AuNRs)$_2$/Cys/Au electrode	0.2 - 200	0.1	0.9998	[53]

4. Conclusion

A novel electrochemical biosensing platform for the $O_2^{\bullet-}$ detection based on biomimetic enzyme self-assembled onto the surface of Fe_3O_4@PS/PDA/SiO_2 nanotubes has been successfully developed. This proposed biosensing platform provided good electrochemical performance because of the constructed nanostructured hybrid nanotubes and self-assembled ($Mn_3(PO_4)_2$). Furthermore, the

biosensor displayed high selectivity of $O_2^{\bullet-}$ in the presence of related interferences, such as UA, DA, Cys, AA and H_2O_2. Besides high selectivity, the present $O_2^{\bullet-}$ biosensor with high specific surface area exhibited excellent analytical performance, such as wider linear range, good cycle stability, compared to the previous $O_2^{\bullet-}$ biosensors. The satisfactory test results of the actual sample analysis indicated that the biosensor we fabricated had a great potential for practical application.

Acknowledgements

The work was supported by National Natural Science Foundation of China (51641104, 21603105, 21571104), Jiangsu Key Technology RD Program (BE2016010), Huaian Key Research and Development Program (HAG201621), the Priority Academic Program Development of Jiangsu Higher Education Institution, and Major projects of Natural Sciences of University in Jiangsu Province of China (14KJA150006, 15KJA350002).

References

[1] Y. Zhou, J. Ding, T. Liang, E.S. Abdel-Halim, L. Jiang, J.-J. Zhu, FITC Doped rattle-type silica colloidal particle-based ratiometric fluorescent sensor for biosensing and imaging of superoxide anion, ACS Appl. Mater. Inter. 8 (2016) 6423-6430.

[2] W. Zhang, P. Li, F. Yang, X. Hu, C. Sun, W. Zhang, D. Chen, B. Tang, Dynamic and reversible fluorescence imaging of superoxide anion fluctuations in live cells and in vivo, J. Am. Chem. Soc. 135 (2013) 14956-14959.

[3] M. Pesce, A. Rizzuto, I. La Fratta, R. Tatangelo, G. Campagna, M. Iannasso, A.

Ferrone, S. Franceschelli, L. Speranza, A. Patruno, M.A. De Lutiis, M. Felaco, A. Grilli, Super-oxide anion production and antioxidant enzymatic activities associated with the executive functions in peripheral blood mononuclear cells of healthy adult samples, Neurosci. Res. 106 (2016) 23-28.

[4] Zhu, T. Liu, H. Zhao, L. Shi, X. Li, M. Lan, Ultrasensitive detection of superoxide anion released from living cells using a porous Pt–Pd decorated enzymatic sensor, Biosens. Bioelectron. 79 (2016) 449-456.

[5] Z. Deng, Q. Rui, X. Yin, H. Liu, Y. Tian, In vivo detection of superoxide anion in bean sprout based on ZnO nanodisks with facilitated activity for direct electron transfer of superoxide dismutase, Anal. Chem. 80 (2008) 5839-5846.

[6] J. Márquez, L.F. Cházaro-Ruiz, L. Zimányi, G. Palestino, Immobilization strategies and electrochemical evaluation of porous silicon based cytochrome c electrode, Electrochimica Acta, 140 (2014) 550-556.

[7] M. Ganesana, J.S. Erlichman, S. Andreescu, Real-time monitoring of superoxide accumulation and antioxidant activity in a brain slice model using an electrochemical cytochrome c biosensor, Free Radical Biol. Med. 53 (2012) 2240-2249.

[8] X. Ji, J. Ren, J. Jin, T. Nakamura, A sensor for superoxide in aqueous and organic/aqueous media based on immobilized cytochrome c on binary self-assembled monolayers, Biosens. Bioelectron. 23 (2007) 241-247.

[9] M. Braik, M.M. Barsan, C. Dridi, M. Ben Ali, C.M.A. Brett, Highly sensitive amperometric enzyme biosensor for detection of superoxide based on conducting

polymer/CNT modified electrodes and superoxide dismutase, Sens. Actuators. B, Chem. 236 (2016) 574-582.

[10] X. Ma, W. Hu, C. Guo, L. Yu, L. Gao, J. Xie, C.M. Li, DNA-templated biomimetic enzyme sheets on carbon nanotubes to sensitively in situ detect superoxide anions released from cells, Adv. Funct. Mater. 24 (2014) 5897-5903.

[11] H. Wei, E. Wang, Nanomaterials with enzyme-like characteristics (nanozymes): next-generation artificial enzymes, Chem. Soc. Rev. 42 (2013) 6060-6093.

[12] M.-Q. Wang, C. Ye, S.-J. Bao, M.-W. Xu, Y. Zhang, L. Wang, X.-Q. Ma, J. Guo, C.-M. Li, Nanostructured cobalt phosphates as excellent biomimetic enzymes to sensitively detect superoxide anions released from living cells, Biosens. Bioelectron. 87 (2017) 998-1004.

[13] T. Liu, X. Niu, L. Shi, X. Zhu, H. Zhao, M. Lana, Electrocatalytic analysis of superoxide anion radical using nitrogen-doped graphene supported Prussian Blue as a biomimetic superoxide dismutase, Electrochim. Acta. 176 (2015) 1280-1287.

[14] R.L. McNaughton, A.R. Reddi, M.H.S. Clement, A. Sharma, K. Barnese, L. Mn^{2+} speciation and oxidative stress resistance in yeast cells with electron-nuclear double resonance spectroscopy, Proc. Natl. Acad. Sci. U.S.A. 107 (2010) 15335-15339.

[15] K. Barnese, E.B. Gralla, J.S. Valentine, D.E. Cabelli, Biologically relevant mechanism for catalytic superoxide removal by simple manganese compounds, Proc. Natl. Acad. Sci. U.S.A. 109 (2012) 6892-6897.

[16] K. Barnese, E.B. Gralla, D.E. Cabelli, J. Selverstone Valentine, Manganous phosphate acts as a superoxide dismutase, J. Am. Chem. Soc. 130 (2008) 4604-4606.

[17] Y. Luo, Y. Tian, Q. Rui, Electrochemical assay of superoxide based on biomimetic enzyme at highly conductive TiO_2 nanoneedles: from principle to applications in living cells, Chem. Commun. (2009) 3014-3016.

[18] J. Zhou, Y. Luo, A. Zhu, Y. Liu, Z. Zhu, Y. Tian, A reliable and durable approach for real-time determination of cellular superoxide anion based on biomimetic superoxide dismutase stabilized by a zeolite, Analyst 136 (2011) 1594-1598.

[19] Y. Luo, G. Hu, A. Zhu, B. Kong, Z. Wang, C. Liu, Y. Tian, A biomimetic sensor for the determination of extracellular O_2^- using synthesized Mn-TPAA on TiO_2 nanoneedle film, Biosens. Bioelectron. 29 (2011) 189-194.

[20] F.X. Hu, Y.J. Kang, F. Du, L. Zhu, Y.H. Xue, T. Chen, L.M. Dai, C.M. Li, Living cells directly growing on a DNA/$Mn_3(PO_4)_2$-immobilized and vertically aligned CNT array as a free-standing hybrid film for highly sensitive in situ detection of released superoxide anions, Adv. Funct. Mater. 25 (2015) 5924-5932.

[21] X. Shen, Q. Wang, Y. Liu, W. Xue, L. Ma, S. Feng, M. Wan, F. Wang, C. Mao, Manganese phosphate self-assembled nanoparticle surface and its application for superoxide anion detection, Sci. Rep. 6 (2016) 28989.

[22] G. Song, X. She, Z. Fu, J. Li, Preparation of good mechanical property polystyrene nanotubes with array structure in anodic aluminum oxide template using simple physical techniques, J. Mater. Res. 19 (2004) 3324-3328.

[23] K. Kondo, T. Kida, Y. Ogawa, Y. Arikawa, M. Akashi, Nanotube formation through the continuous one-dimensional fusion of hollow nanocapsules composed of layer-by-layer poly(lactic acid) stereocomplex films, J. Am. Chem. Soc. 132 (2010) 8236-8237.

[24] C. Yang, L. Zhang, N. Hu, Z. Yang, Y. Su, S. Xu, M. Li, L. Yao, M. Hong, Y. Zhang, Rational design of sandwiched polyaniline nanotube/layered graphene/polyaniline nanotube papers for high-volumetric supercapacitors, Chem. Eng. J. 309 (2017) 89-97.

[25] R. Ren, C. Leng, S. Zhang, A chronocoulometric DNA sensor based on screen-printed electrode doped with ionic liquid and polyaniline nanotubes, Biosens. Bioelectron. 25 (2010) 2089-2094.

[26] M. Steinhart, J.H. Wendorff, A. Greiner, R.B. Wehrspohn, K. Nielsch, J. Schilling, J. Choi, U. Gosele, Polymer nanotubes by wetting of ordered porous templates, Science. 296 (2002) 1997.

[27] S. Sun, L. Chen, H. Shi, Y. Li, X. He, Magnetic glass carbon electrode, modified with magnetic ferriferrous oxide nanoparticles coated with molecularly imprinted polymer films for electrochemical determination of bovine hemoglobin, J. Electroanal. Chem. 734 (2014) 18-24.

[28] X. Li, H. Li, G. Liu, Z. Deng, S. Wu, P. Li, Z. Xu, H. Xu, P.K. Chu, Magnetite-loaded fluorine-containing polymeric micelles for magnetic resonance imaging and drug delivery, Biomaterials 33 (2012) 3013-3024.

[29] F. Peng, Q. Wang, R. Shi, Z. Wang, X. You, Y. Liu, F. Wang, J. Gao, C. Mao,

Fabrication of sesame sticks-like silver nanoparticles/polystyrene hybridnanotubes and their catalytic effects, Sci. Rep. 6 (2016) 39502.

[30] G. Chen, R. Chen, C. Zou, D. Yang, Z.-S. Chen, Fragmented polymer nanotubes from sonication-induced scission with a thermo-responsive gating system for anti-cancer drug delivery, J. Mater. Chem. B 2 (2014) 1327-1334.

[31] X. Liu, L. Chen, H. Liu, G. Yang, P. Zhang, D. Han, S. Wang, L. Jiang, Bio-inspired soft polystyrene nanotube substrate for rapid and highly efficient breast cancer-cell capture, NPG Asia Mater. 5 (2013) e63.

[32] H. Lee, S.M. Dellatore, W.M. Miller, P.B. Messersmith, Mussel-inspired surface chemistry for multifunctional coatings, Science 318 (2007) 426-430.

[33] C. Wu, W. Fan, J. Chang, Y. Xiao, Mussel-inspired porous SiO_2 scaffolds with improved mineralization and cytocompatibility for drug delivery and bone tissue engineering, J. Mater. Chem. 21 (2011) 18300-18307.

[34] Y. Yang, S. Qiu, W. Cui, Q. Zhao, X. Cheng, R.K.Y. Li, X. Xie, Y.-W. Mai, A facile method to fabricate silica-coated carbon nanotubes and silica nanotubes from carbon nanotubes templates, J. Mater. Sci. 44 (2009) 4539-4545.

[35] W. Zhao, K. Wang, Y. Wei, Y. Ma, L. Liu, X. Huang, Laccase biosensor based on phytic acid modification of nanostructured SiO_2 surface for sensitive detection of dopamine, Langmuir 30 (2014) 11131-11137.

[36] L. Yuan, S. Liu, W. Tu, Z. Zhang, J. Bao, Z. Dai, Biomimetic superoxide dismutase stabilized by photopolymerization for superoxide anions biosensing and cell monitoring, Anal. Chem. 86 (2014) 4783-4790.

[37] Y. Cong, T. Xia, M. Zou, Z. Li, B. Peng, D. Guo, Z. Deng, Mussel-inspired polydopamine coating as a versatile platform for synthesizing polystyrene/Ag nanocomposite particles with enhanced antibacterial activities, J. Mater. Chem. B 2 (2014) 3450-3461.

[38] W. Wang, Y. Jiang, S. Wen, L. Liu, L. Zhang, Preparation and characterization of polystyrene/Ag core-shell microspheres-a bio-inspired poly(dopamine) approach, J. Colloid Interface Sci. 368 (2012) 241-249.

[39] Z. Zhang, C. Shao, Y. Sun, J. Mu, M. Zhang, P. Zhang, Z. Guo, P. Liang, C. Wang, Y. Liu, Tubular nanocomposite catalysts based on size-controlled and highly dispersed silver nanoparticles assembled on electrospun silica nanotubes for catalytic reduction of 4-nitrophenol, J. Mater. Chem. 22 (2012) 1387-1395.

[40] M. Llusar, C. Sanchez, Inorganic and hybrid nanofibrous materials templated with organogelators, Chem. Mater. 20 (2008) 782-820.

[41] L. Yang, H. Liu, N. Hu, Assembly of electroactive layer-by-layer films of myoglobin and small-molecular phytic acid, Electrochem. Commun. 9 (2007) 1057-1061.

[42] J. Dong, Y. Wen, Y. Miao, Z. Xie, Z. Zhang, H. Yang, A nanoporous zirconium phytate film for immobilization of redox protein and the direct electrochemical biosensor, Sens. Actuators, B-Chem. 150 (2010) 141-147.

[43] B. Fei, B. Qian, Z. Yang, R. Wang, W.C. Liu, C.L. Mak, J.H. Xin, Coating carbon nanotubes by spontaneous oxidative polymerization of dopamine, Carbon 46 (2008) 1795-1797.

[44] C.-C. Ho, S.-J. Ding, The pH-controlled nanoparticles size of polydopamine for anti-cancer drug delivery, J. Mater. Sci. - Mater. Med. 24 (2013) 2381-2390.

[45] V.K.S. Hsiao, J.R. Waldeisen, Y. Zheng, P.F. Lloyd, T.J. Bunning, T.J. Huang, Aminopropyltriethoxysilane (APTES)-functionalized nanoporous polymeric gratings: fabrication and application in biosensing, J. Mater. Chem. 17 (2007) 4896-4901.

[46] W. Zhao, Y. Ni, Q. Zhu, R. Fu, X. Huang, J. Shen, Innovative biocompatible nanospheres as biomimetic platform for electrochemical glucose biosensor, Biosens. Bioelectron. 44 (2013) 1-5.

[47] S. Stankovich, D.A. Dikin, G.H.B. Dommett, K.M. Kohlhaas, E.J. Zimney, E.A. Stach, R.D. Piner, S.T. Nguyen, R.S. Ruoff, Graphene-based composite materials, Nature 442 (2006) 282-286.

[48] G. Preda, A. Migani, K.M. Neyman, S.T. Bromley, F. Illas, G. Pacchioni, Formation of superoxide anions on ceria nanoparticles by interaction of molecular oxygen with Ce^{3+} sites, J. Phys. Chem. C. 115 (2011) 5817-5822.

[49] C. Amatore, S. Arbault, A.C.W. Koh, Simultaneous detection of reactive oxygen and nitrogen species released by a single macrophage by triple potential-step chronoamperometry, Anal. Chem. 82 (2010) 1411-1419.

[50] H.M. Peshavariya, G.J. Dusting, S. Selemidis, Analysis of dihydroethidium fluorescence for the detection of intracellular and extracellular superoxide produced by NADPH oxidase, Free Radical Res. 41 (2007) 699-712.

[51] X. Zhu, X. Niu, H. Zhao, J. Tang, M. Lan, Immobilization of superoxide

dismutase on Pt–Pd/MWCNTs hybrid modified electrode surface for superoxide anion detection, Biosens. Bioelectron. 67 (2015) 79-85.

[52] P. Santhosh, K.M. Manesh, S.-H. Lee, S. Uthayakumar, A.I. Gopalan, K.-P. Lee, Sensitive electrochemical detection of superoxide anion using gold nanoparticles distributed poly(methyl methacrylate)-polyaniline core-shell electrospun composite electrode, Analyst 136 (2011) 1557-1561.

[53] M. Wang, Y. Han, X. Liu, Z. Nie, C. Deng, M. Guo, S. Yao, Assembly of layer-by-layer films of superoxide dismutase and gold nanorods: A third generation biosensor for superoxide anion, Sci. Chi. Chem. 54 (2011) 1284.

Table 1. Comparison of the analytical performance of various electrodes for $O_2^{\bullet-}$ detection.

Electrode	Linear range (μM)	Detection Limit (μM)	Correlation coefficient	Ref.
Fe_3O_4@PS/PDA/SiO_2-$Mn_3(PO_4)_2$ /MWCNTs/MGCE	0.15 - 3.0	0.0136	0.9976	This work
Mn^{2+}-ZSM/PDDA/GCE	0.5 - 1200	0.37	-	[18]
MWCNTs/$Mn_2P_2O_7$-formylstyrylpyridine/GCE	0.08 - 3.19	0.029	0.9915	[36]
SOD/Pt-Pd/MWCNTs/SPGE	40 - 1550	0.71	0.9941	[51]
PMMA/PANI-Au_{nano}/SOD-ESCFM	0.5 - 2.4	0.3	0.9944	[52]
((SOD/AuNRs)$_2$/Cys/Au	0.2 - 200	0.1	0.9998	[53]

electrode

Highlights

- The sensor based on magnetic polystyrene nanotubes decorated with $Mn_3(PO_4)_2$ nanoparticles for detection of superoxide anion.
- $Mn_3(PO_4)_2$ nanoparticles were self-assembled on the surface of magnetic polystyrene nanotubes rather than $Mn_3(PO_4)_2$ nanosheets.
- The biosensor exhibited excellent analytical performance for detection of superoxide anion.

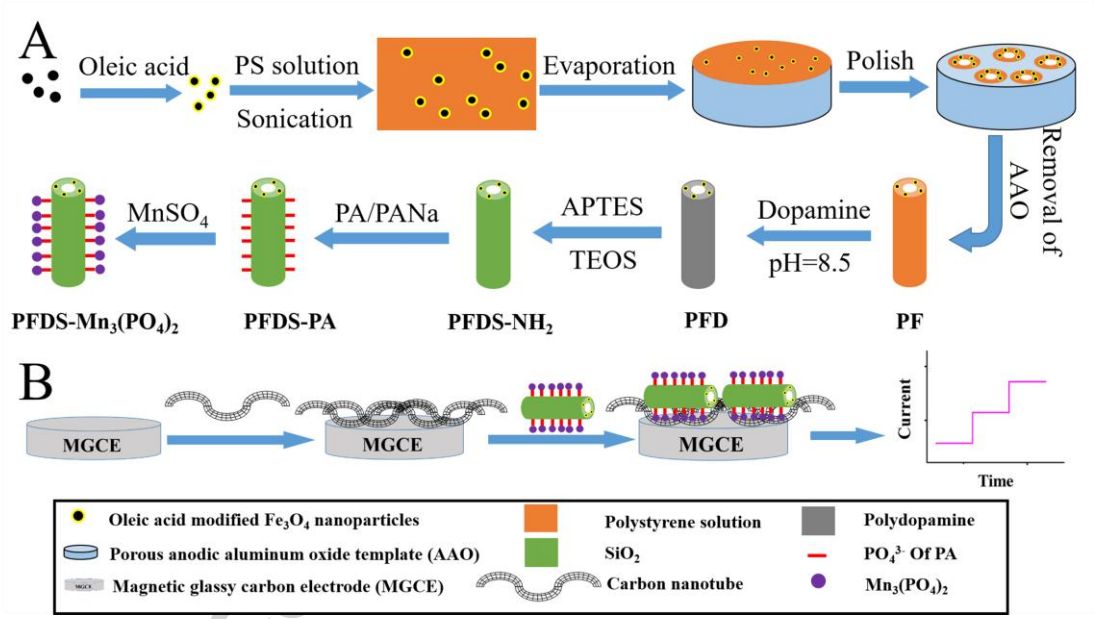

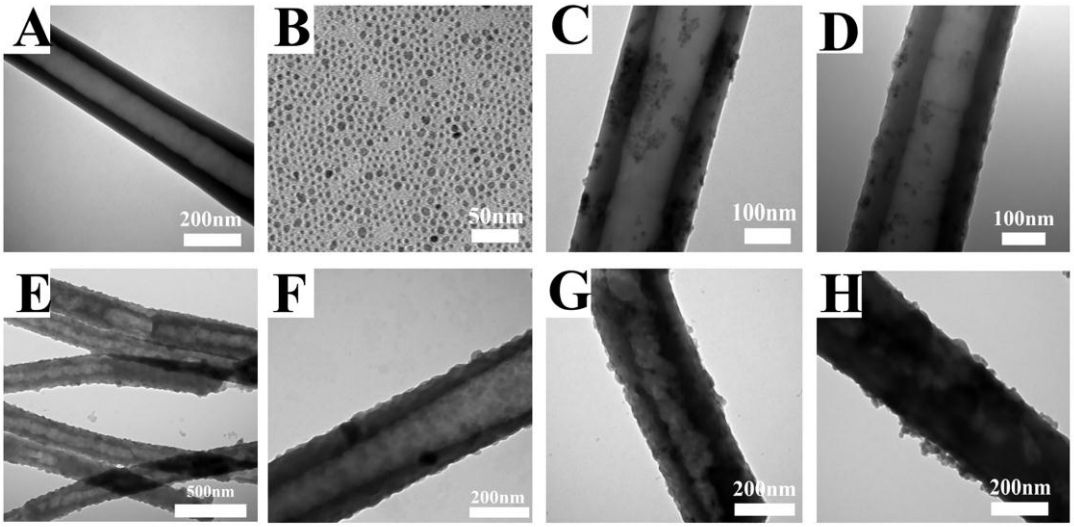
A
200nm
B
50nm
C
100nm
D
100nm
E
500nm
F
200nm
G
200nm
H
200nm

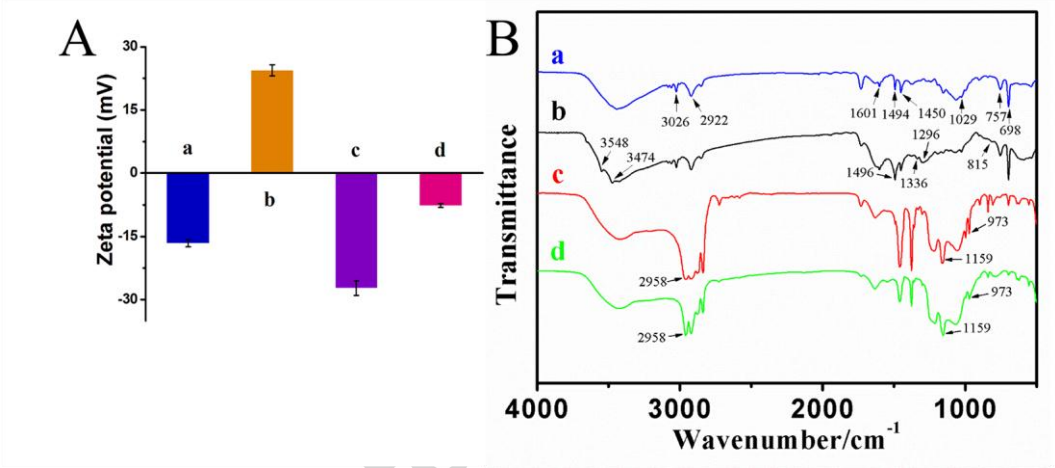
A
Zeta potential (mV)
30
15
0
-15
-30
a
b
c
d
B
Transmittance
a
b
c
d
3026
2922
1601
1494
1450
1029
757
698
3548
3474
1296
1496
1336
815
973
1159
2958
973
1159
2958
4000
3000
2000
1000
Wavenumber/cm-1

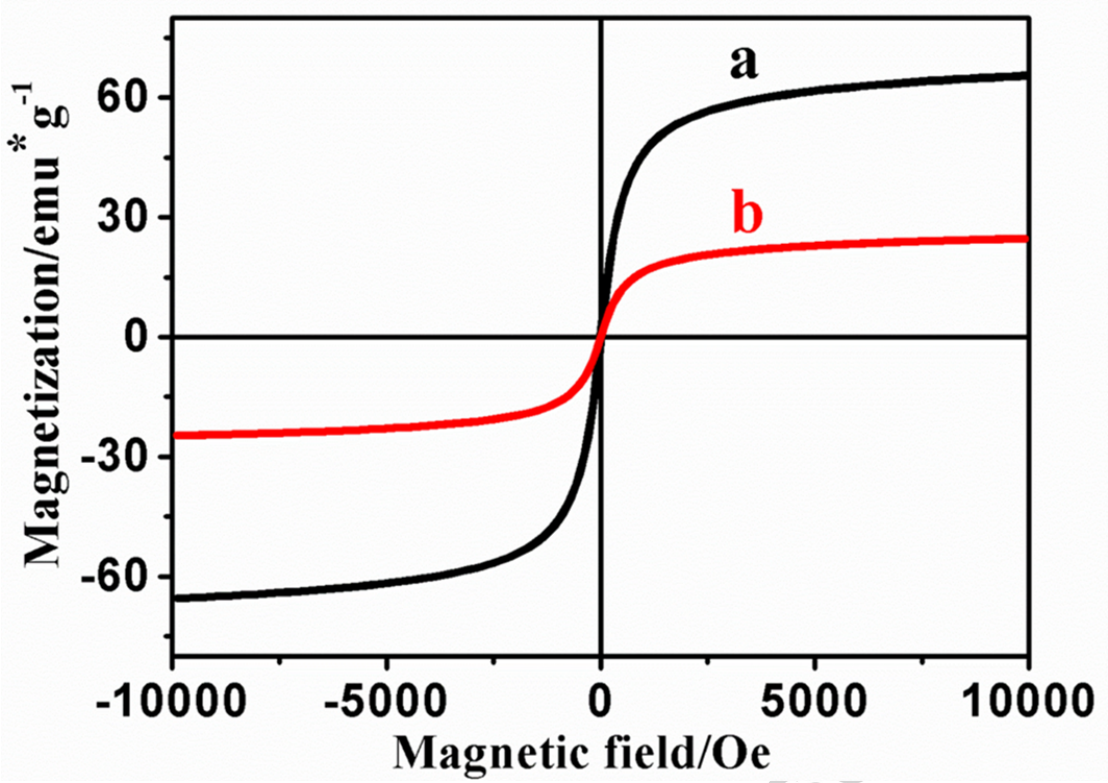

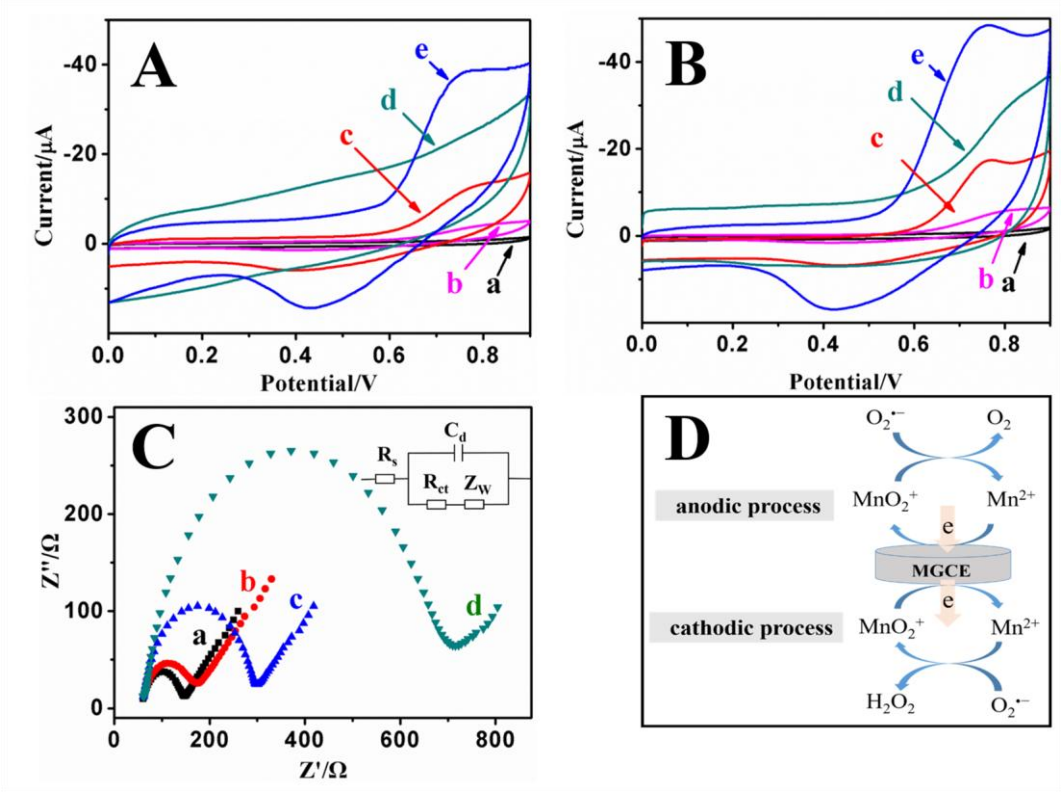

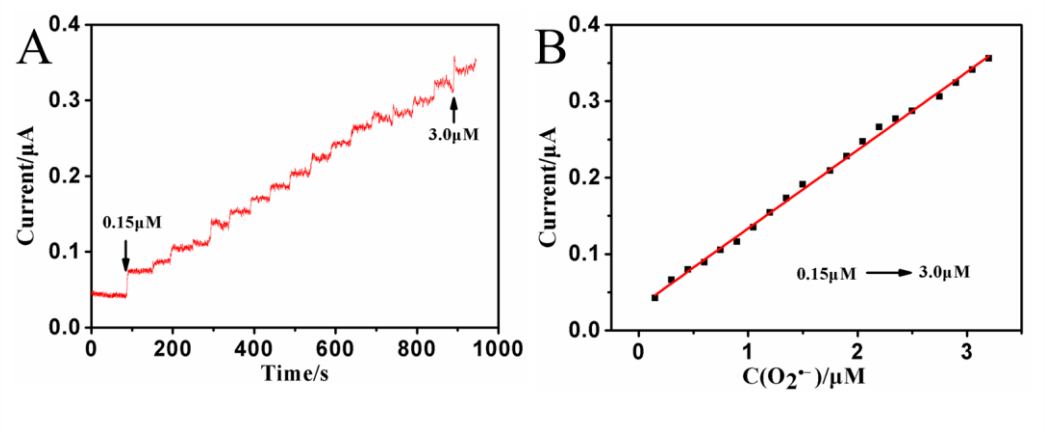
A
Current/μA
Time/s
0.15μM
3.0μM
B
Current/μA
C(O2•−)/μM
0.15μM → 3.0μM

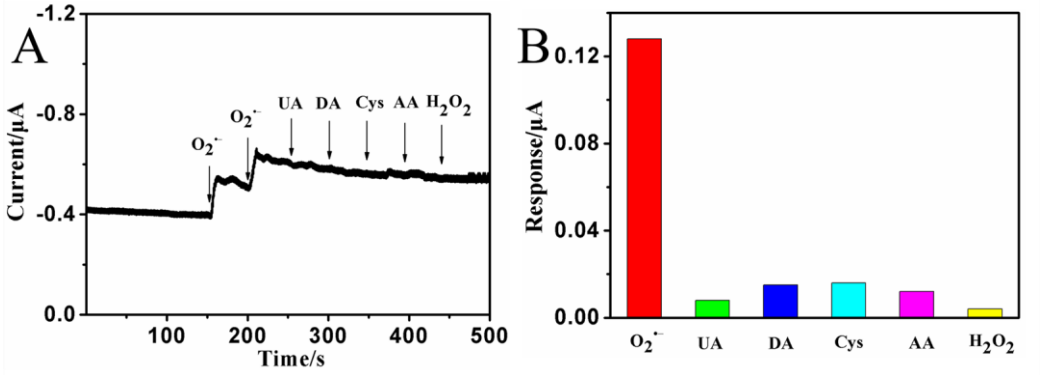
A
Current/μA
Time/s
O2•−
O2•−
UA
DA
Cys
AA
H2O2
B
Response/μA
O2•−
UA
DA
Cys
AA
H2O2

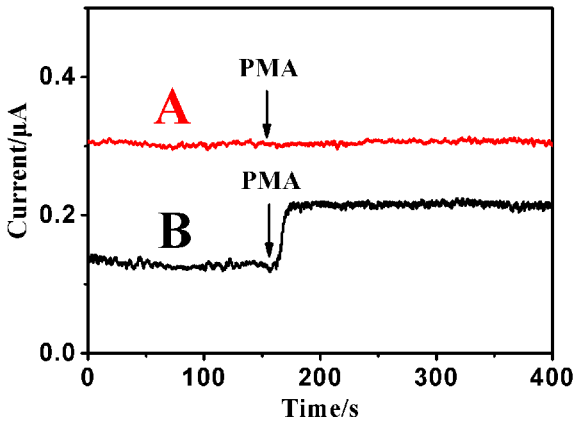
Current/μA
Time/s
PMA
A
PMA
B